THE JOURNAL OF PHYSICAL CHEMISTRY C
A JOURNAL OF THE AMERICAN CHEMICAL SOCIETY

pubs.acs.org/JPCC
Article

Properties of Erythritol Tetranitrate from Molecular Dynamics Simulation

M. J. Cawkwell* and V. W. Manner

Cite This: J. Phys. Chem. C 2024, 128, 5749−5758
Read Online

ACCESS | Metrics & More | Article Recommendations | Supporting Information

ABSTRACT: The nonpolarizable force field for alkyl nitrates developed by Borodin et al. [*J. Phys. Chem. B*, **2008**, *112*, 734−742] has been employed to calculate selected properties of crystalline and liquid erythritol tetranitrate (ETN). The set of partial charges proposed by Borodin for pentaerythritol tetranitrate (PETN) was used except for a small correction to the H atom charges to ensure charge neutrality owing to the absence of the neopentyl carbon in ETN. The force field was used to compute the isothermal compression curve, lattice parameters, heat capacity, thermal expansivity, single crystal elastic constants, and Gruneisen parameters of crystalline ETN. The density- and temperature-dependent viscosities of liquid ETN are also reported. We anticipate that these data will be of some utility to the development of equations of state and thermomechanical models for ETN.

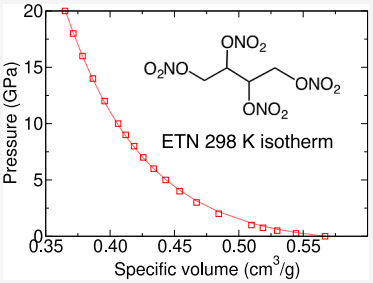

1. INTRODUCTION

Erythritol tetranitrate, ETN, $C_4H_6N_4O_{12}$, is a powerful and somewhat sensitive explosive that can be melt-casted.[1−4] It is related chemically to other nitrate ester-containing explosives such as pentaerythritol tetranitrate (PETN) and nitroglycerin, as illustrated in Figure 1. It adopts a monoclinic unit cell in the

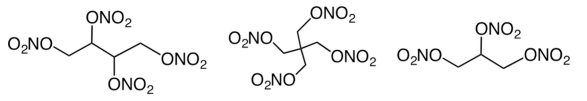

Figure 1. Structures of erythritol tetranitrate (ETN), pentaerythritol tetranitrate (PETN), and nitroglycerin (NG).

space group $P2_1/c$ with a density of 1.77 g cm^{-3} at room temperature.[5] The excellent explosive performance and widespread availability of the precursor compound, erythritol, has led to renewed interest in this molecule.[6] Homemade explosive applications have increased in recent years along with a wealth of forensic analysis studies.[7−10] Oxley and co-workers have recently examined the thermal decomposition of ETN through both experimental and computational methods[11] and our group has evaluated its decomposition kinetics under low pressure, drop weight impact conditions.[12,13] ETN is one of a suite of aliphatic nitrate ester explosives that lend themselves to experimental and computational studies that increase our understanding of explosive decomposition mechanisms.[14]

The poor handling sensitivity of ETN makes it impractical for standard commercial applications,[15] but in our laboratories, it has become useful for evaluating stimuli that would be unlikely to elicit a reaction from more insensitive energetic materials.[16] Because of its potential value in understanding initiation mechanisms in small-scale safety tests, we have computed a subset of its properties that are pertinent to the development of thermomechanical models. These properties include its isothermal compression curve, lattice parameters, thermal expansivity, heat capacity, single crystal elastic constants, and liquid density and viscosity. The calculations have been performed using molecular dynamics (MD) simulations with an empirical force field developed originally for PETN.[17] This force field has been modified slightly for ETN and the predictions from the simulations have been validated against results from semiempirical and density functional theory (DFT) calculations or experiment where possible.

2. FORCE FIELD FOR ALKYL NITRATES

The MD simulations used the nonpolarizable, nonreactive force field for alkyl nitrates that was developed originally by Borodin and co-workers.[17] The force field represents bond stretches, bends, and dihedral and improper torsions using sums of harmonic springs that were parametrized to the results of DFT calculations. The expressions used to represent the intramolecular forces are

$$u_{\alpha\beta}^{bond}(R_{ab}) = \frac{1}{2}k_{\alpha\beta}^{bond}(R_{ab} - R_{\alpha\beta}^{0})^2 \quad (1)$$

$$u_{\alpha\beta}^{bend}(\theta_{abc}) = \frac{1}{2}k_{\alpha\beta\gamma}^{bend}(\theta_{abc} - \theta_{\alpha\beta\gamma}^{0})^2 \quad (2)$$

Received: January 24, 2024
Revised: March 7, 2024
Accepted: March 12, 2024
Published: March 21, 2024

https://doi.org/10.1021/acs.jpcc.4c00489
J. Phys. Chem. C 2024, 128, 5749−5758

$$u^{dih}_{\alpha\beta\gamma\delta}(\phi_{abcd}) = \frac{1}{2}\sum_n k^{dih}_{\alpha\beta\gamma\delta}[1 - \cos(n\phi_{abcd})] \quad (3)$$

and

$$u^{imp}_{\alpha\beta\gamma\delta}(\chi_{abcd}) = \frac{1}{2}k^{imp}_{\alpha\beta\gamma\delta}(\chi_{abcd})^2 \quad (4)$$

where a, b, c, and d label atoms, α, β, γ, and δ label atom types, R_{ab} is the distance between atoms a and b, θ_{abc} is the angle made by the bonds between atoms a and b and atoms b and c, and ϕ_{abcd} and χ_{abcd} are the dihedral and out-of-plane angle between atoms a, b, c, and d, respectively. Only sets of atoms forming direct, first-nearest-neighbor bonds are included in the terms for the potential energy. $R^0_{\alpha\beta}$ and $\theta^0_{\alpha\beta\gamma}$ are the equilibrium bond distances and angles between atom types α, β, and γ, respectively, which along with the set of spring constants, k, are parametrized to DFT calculations. Nonbonded interactions are described by sums of atom-centered Buckingham potentials that take the form

$$u^{nb}(R_{ab}) = A_{\alpha\beta}\exp(-B_{\alpha\beta}R_{ab}) - C_{\alpha\beta}/R^6_{ab} \quad (5)$$

where $a \in \alpha$, $b \in \beta$, and A, B, and C are adjustable parameters that are parametrized for interactions between like atoms, $\alpha = \beta$. The Waldman−Hagler rules are used to derive the corresponding parameters between unlike atoms, $\alpha \neq \beta$,

$$A_{\alpha\beta} = (A_{\alpha\alpha}A_{\beta\beta})^{1/2}\frac{B^6_{\alpha\beta}}{B^3_{\alpha\alpha}B^3_{\beta\beta}} \quad (6)$$

$$B_{\alpha\beta} = \left(\frac{2}{B^{-6}_{\alpha\alpha} + B^{-6}_{\beta\beta}}\right)^{1/6} \quad (7)$$

and

$$C_{\alpha\beta} = (C_{\alpha\alpha}C_{\beta\beta})^{1/2} \quad (8)$$

We have not included the R^{-12} term in the nonbonded term from the Borodin force field that provides strong short-range repulsion because in this study we do not access dynamic high pressure conditions. Electrostatic interactions are included via a set of atom-centered partial charges, $\{q\}$. Nonbonded and electrostatic interactions between first and second nearest neighbor atoms are excluded from the potential energy and forces.

The Borodin force field was implemented in the LAMMPS MD code[18,19] and an example input deck is provided with the Supporting Information. The long-range electrostatic interactions were calculated using the particle−particle, particle-mesh (PPPM) algorithm[20] under three-dimensional periodic boundary conditions, and a time step for the integration the equations of motion of 0.25 fs was used for all simulations.

The parameters for the intramolecular forces and nonbonded interactions were taken as-is from ref 17. The set of partial charges for the nonpolarizable force field tabulated in ref 17 were derived for a neutral PETN molecule. In the Borodin force field, the charge on the center neopentyl carbon in PETN, $q = -0.3344$ e, differs significantly from that on the $-CH_2-$ carbons, $q = 0.3034$ e. The absence of the neopentyl carbon atom in ETN means that the set of partial charges must be revised relative to those of PETN so that the molecule remains charge neutral. We opted to set the partial charges on the primary and secondary carbons in ETN to those derived for the $-CH_2-$ carbons in PETN, that is $q = 0.3034$ e, and then adjusted the charges of the hydrogen atoms to achieve charge neutrality. The updated set of partial charges for ETN is provided in Table 1. The self-consistent Mulliken partial charges on the primary and secondary carbon atoms calculated at the optimized gas-phase geometry using density functional tight binding (DFTB) theory[21] differ by only 0.01 e, which suggests that the simplifying approximation of using the same partial charges on the four carbon atoms will have a negligible effect on the overall accuracy of the electrostatic forces.

Table 1. Partial Charges for ETN Derived from the Borodin Force Field

atom type	partial charges (e)
C	0.3034
H	0.035667
N	0.8642
nitrate O	−0.4171
nitro O	−0.4020

3. EVALUATION OF PHYSICAL PROPERTIES OF CRYSTALLINE AND LIQUID ETN

3.1. Isothermal Compression, Lattice Parameters, and Thermal Expansivity. The ability of the Borodin force field to describe the structure of the ETN crystal lattice was evaluated by computing its density and lattice parameters as a function of the temperature and pressure. These properties are compared against experimental measurements and data calculated using dispersion-corrected DFT. The MD and DFT simulations of crystalline ETN all used the monoclinic crystal structure derived from single crystal X-ray diffraction at 140 K by Manner et al. as the initial geometry (Cambridge Structural Database refcode YOYSUC).[5] All of the MD simulations of crystalline ETN with the Borodin force field were performed using a $3 \times 9 \times 3$ supercell containing 8424 atoms to mitigate the effects of self-interactions over periodic boundaries. The temperature and pressure in the simulations were controlled by using a single Nose−Hoover thermostat and barostat. The barostat was allowed to update the lengths and angles of the periodic simulation cell independently to ensure that hydrostatic conditions were achieved.

Density functional theory calculations of the ETN cold curve and the dependence of the lattice parameters on hydrostatic pressure were performed using the Gaussian Plane Waves (GPW) method in the CP2k package[22] with the PBE generalized gradient approximation exchange-correlation functional,[23] a TZVP basis set, Goedecker−Teter−Hutter pseudopotentials,[24] and the D3(BJ) dispersion correction.[25] The plane wave and relative cutoff energies were set to 1200 and 60 Ry, respectively, and the integration over the first Brillouin zone used a $1 \times 3 \times 1$ Monkhorst−Pack k-point mesh.[26] The lattice vectors of the unit cell and the internal coordinates were optimized until the target hydrostatic pressure was achieved to within a tolerance of 0.01 GPa and the maximum force acting on any atom was less than 1×10^{-6} Hartree/a_0. The tolerance for the self-consistent field (SCF) in the calculation of the ground state charge density at each optimization step was set to 10^{-7}.

Table 2 presents the lattice parameters and densities of single crystal ETN at 100, 140, and 291 K and zero pressure from experiment, the Borodin force field, and zero temperature

https://doi.org/10.1021/acs.jpcc.4c00489
J. Phys. Chem. C 2024, 128, 5749−5758

Table 2. Comparison of the Lattice Parameters and Densities of ETN at Zero Pressure from Experiment, MD Simulations Using the Borodin Force Field, and Static Dispersion-Corrected DFT

	100 K		140 K		291 K		298 K		
	expt.[30]	MD	expt.[5]	MD	expt.[30]	MD	expt.[5]	MD	DFT
a (Å)	15.909	16.05	15.893	16.07	16.131	16.11	16.132	16.11	16.285
b (Å)	5.171	5.21	5.160	5.25	5.326	5.44	5.314	5.45	5.264
c (Å)	14.768	14.34	14.731	14.35	14.849	14.38	14.789	14.38	14.920
β (degree)	116.15	116.0	116.16	116.0	116.56	115.8	116.78	115.8	115.55
ρ_0 (g/cm^3)	1.840	1.861	1.851	1.844	1.759	1.768	1.773	1.764	1.739

dispersion-corrected DFT. The results from the MD simulations were obtained by first thermalizing the systems for 10^6 time steps at each target temperature and pressure in the isothermal−isobaric ensemble. Following the thermalization step, the lattice parameters were computed from the time averages of the lattice vectors over an additional run of 10^6 time steps. The agreement between the lattice parameters measured at room temperature and those predicted by the Borodin force field is generally very good, with errors consistent with those seen for other energetic molecular crystals with this type of nonreactive force field (see, for example, refs 27−29). The maximum discrepancies are associated with the b and c lattice parameters, which deviate from the experimental values by about 2.5% and −2.5%, respectively. The errors in the ETN lattice parameters derived from the dispersion-corrected DFT calculations differ by no more than 1% from those measured at room temperature. Nevertheless, despite the absence of any thermal pressure in the static DFT calculations, the equilibrium density, ρ_0, is significantly smaller than those measured at both room and cryogenic temperatures. This discrepancy suggests that the combination of TZVP basis set and D3(BJ) dispersion correction exhibits relatively poor transferability to this system.

The 298 K isothermal compression curve of single crystal ETN computed from the Borodin force field up to 20 GPa and the cold curve computed from dispersion-corrected DFT up to 10 GPa are presented in Figure 2. For a given pressure, the densities on the room temperature isothermal compression curve are systematically larger than those on the DFT-generated cold curve by about 3%.

The isothermal compression curves can be represented accurately by the MACAW reference curve that was proposed recently by Lozano and Aslam.[31,32] The MACAW reference curve is particularly useful for hydrocode simulations because unlike other empirical equations of state, it does not lead to negative bulk moduli when the material is put into tension, and it can be inverted analytically. The MACAW reference curve takes the form

$$P = A\left(\frac{V}{V_0}\right)^{-(B+1)} \exp\left(\frac{2}{3}C\left(1-\left(\frac{V}{V_0}\right)^{3/2}\right)\right)\left(C\left(\frac{V}{V_0}\right)^{3/2}+B\right) - A(B+C) \quad (9)$$

where P is the pressure, V the specific volume, V_0 the specific volume where $P = 0$, and A, B, and C are adjustable parameters. The MACAW reference curve was fitted to the MD and DFT data in Figure 2 by a least-squares optimization of the A and C parameters with $V_0 = 1/\rho_0$ from Table 2 and the parameter B equal to its lower bound, 45/29. The best-fit parameters and the isothermal bulk modulus,

$$K_0 = A\left(B - \frac{1}{2}C + (B+C)^2\right) \quad (10)$$

and its pressure derivative

$$K_0' = B + C - 2 + \frac{3}{4}\left[\frac{4B(B+C+1) - C}{B - C/2 + (B+C)^2}\right] \quad (11)$$

derived from the MACAW fit are given in Table 3.

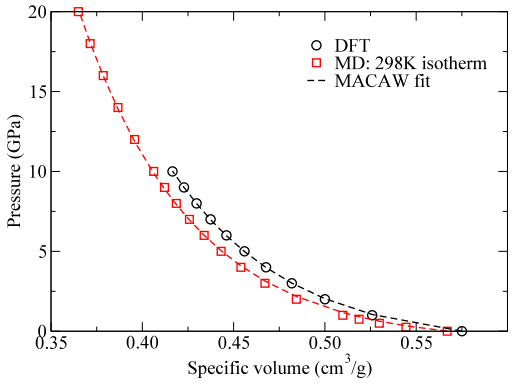

Figure 2. 298 K isothermal compression computed from the Borodin force field and the cold curve computed from dispersion-corrected DFT. The broken lines depict the best fits of the MACAW reference curve to the data.

The dependences of the ETN lattice parameters on hydrostatic pressure computed from the Borodin force field at 298 K and from static DFT are presented in Figure 3. The changes in the four lattice parameters with increasing hydrostatic pressure are clearly consistent between the MD and DFT calculations, although the Borodin force field appears to slightly underestimate the change in the monoclinic β angle.

The volumetric and anisotropic linear coefficients of thermal expansion were computed between 50 and 500 K by using a series of isothermal−isobaric MD simulations at zero pressure. The three coefficients of linear expansion, α_a, α_b, and α_{c^*}, were computed from the dependences of the primary lattice vectors on temperature. Because the coefficient of volumetric expansion, α_V, is equal to the sum of the three linear coefficients of thermal expansion, we computed the expansivity along the a = [100], b = [010], and $c^* = a \times b$ directions, where c^* is the component of the [001] lattice vector normal to the (001) plane. The dependences of the volumetric and linear coefficients of thermal expansion on temperature are presented in Figure 4, which clearly highlight the pronounced anisotropies in the linear expansivities. The volumetric expansion coefficient is dominated by linear expansion along b and at temperatures in excess of about 300 K, the lattice is predicted to contract along a and c^*. The magnitude of the predicted volumetric thermal expansivity at room temperature,

https://doi.org/10.1021/acs.jpcc.4c00489
J. Phys. Chem. C 2024, 128, 5749−5758

Table 3. Best Fit Parameters, Isothermal Bulk Moduli, and Pressure Derivatives of the Isothermal Bulk Moduli for the MACAW Reference Curves

	A (GPa)	B (−)	C (−)	V_0 (cm^3/g)	K_0 (GPa)	K_0' (−)
Borodin MD	0.0651648	45/29	8.78915	1/1.764	6.783	8.784
DFT	0.0840504	45/29	8.35439	1/1.739	8.027	8.372

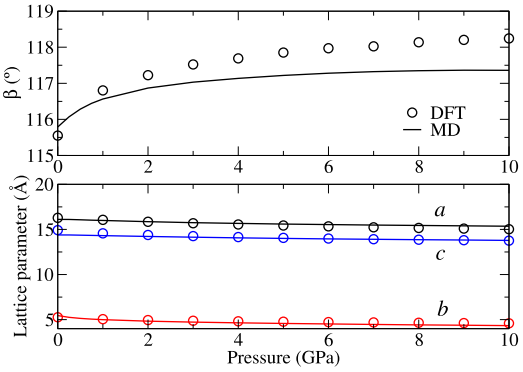

Figure 3. Dependences of the ETN lattice parameters on hydrostatic pressure. The MD results were derived from the 298 K isothermal compression curve, and the DFT results from the cold curve.

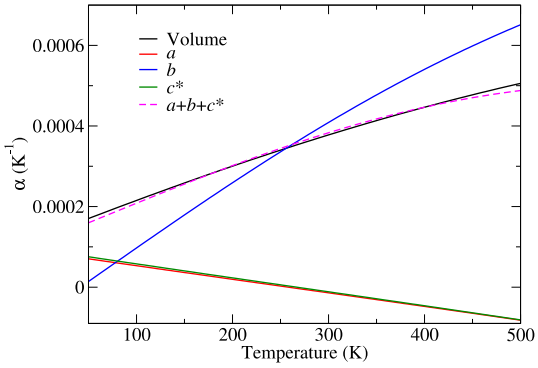

Figure 4. Dependences of the volumetric and anisotropic linear coefficients of thermal expansion on the temperature.

0.00037 K^{-1}, is somewhat larger than those measured for related compounds such as PETN, α_V = 0.00025 K^{-1}, which we attribute in part to the comparatively low melting temperature of ETN with respect to other energetic materials.[33]

3.2. Vibrational Frequencies, Heat Capacity, and Grüneisen Parameter. The vibrational density of states of crystalline ETN, $g(\omega)$, where ω denotes angular frequency, have been computed from the cosine transform of the velocity autocorrelation function, $\gamma(t)$,

$$g(\omega) = \int_0^{\omega_{max}} \gamma(t)\cos(\omega t)\mathrm{d}t \tag{12}$$

where

$$\gamma(t) = \left\langle \frac{1}{N}\sum_{a=1}^{N} \frac{v_a(0)\cdot v_a(t)}{v_a(0)\cdot v_a(0)} \right\rangle \tag{13}$$

N is the number of atoms, $v_a(t)$ is the velocity of atom a at time t, and an average is taken over all time origins. The normalization of the velocity autocorrelation used in eq 13 differs from that proposed originally by Dickey and Paskin,[34] but as discussed in ref 32, it leads to a properly normalized phonon density of states where the integral of each peak corresponds precisely to the number of harmonic distortions of the molecules associated with each set of normal modes. In Figure 5, we plot the phonon density of states, $g(f)$, computed

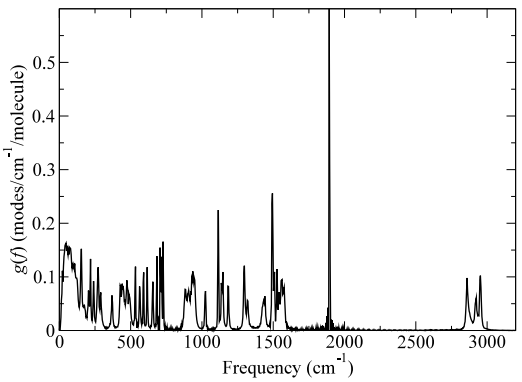

Figure 5. Phonon density of states of single crystal ETN at zero pressure and 300 K from the Borodin force field.

from the time history of the atomic velocities from an MD simulation at zero pressure in the microcanonical ensemble (constant number of particles, volume, and total energy) at 300 K. The phonon density of states has been renormalized such that

$$\int_0^{\infty} g(f)\mathrm{d}f = 3N_{mol} \tag{14}$$

where N_{mol} = 26 is the number of atoms per ETN molecule. As in earlier studies of the vibrational properties of nitrate esters with the Borodin force field we observe a sharp peak in the phonon density of states at about f = 1900 cm^{-1} that was attributed by Pereverzev and Sewell[32] to the antisymmetric NO_2 stretch.

The heat capacity at constant volume, C_V, can be calculated from the phonon density of states via the standard result,

$$C_V(T) = k_B \int_0^{\infty} g(f)\left(\frac{(hf/k_BT)^2\exp(-hf/k_BT)}{(1-\exp(-hf/k_BT))^2}\right)\mathrm{d}f \tag{15}$$

where k_B and h are the Boltzmann and Planck constants, respectively, and T is the temperature.[35] The dependence of the constant volume heat capacity on the temperature at V = 1/1.763 cm^3/g using the phonon density of states in Figure 5 is presented in Figure 6. At room temperature, eq 15 yields C_V = 0.98 J g^{-1} K^{-1}, which, as expected, is consistent with the heat capacities of similar molecular materials.

The dimensionless Grüneisen parameter

$$\Gamma = V\left(\frac{\partial P}{\partial U}\right)_V \tag{16}$$

where U is the internal energy, represents the dependence of the thermal pressure on thermal energy for a system held at constant volume. It is an important term in the parametrization

https://doi.org/10.1021/acs.jpcc.4c00489
J. Phys. Chem. C 2024, 128, 5749−5758

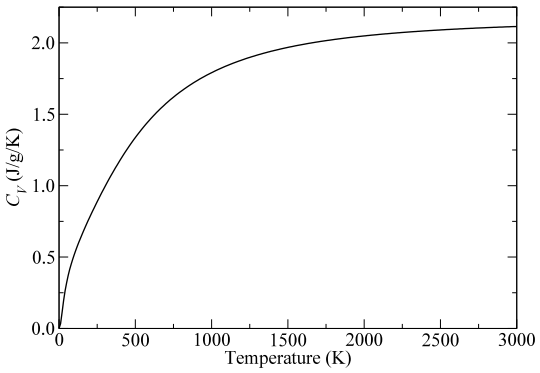

Figure 6. Constant volume heat capacity of single crystal ETN at $V = 1/1.763$ cm^3/g.

of equations of state.[36] It can be calculated from a subset of the properties of single crystal ETN that have been derived from MD simulations using the Borodin force field. One definition for the Grüneisen parameter is

$$\Gamma = \frac{\alpha_V K_0}{\rho C_V} \tag{17}$$

which yields $\Gamma = 0.218$ at ambient pressure and temperature.

The infrared (IR) absorption spectrum of single crystal ETN has been estimated from the time history of the total dipole moment, $M(t)$, from MD simulations with the Borodin force field at ambient density and temperature.[37,38] The IR absorption intensity at angular frequency ω is

$$I(\omega) = \int_0^{\omega_{max}} \left\langle \frac{\dot{M}(0)\cdot\dot{M}(t)}{\dot{M}(0)\cdot\dot{M}(0)} \right\rangle \cos(\omega t)\mathrm{d}t \tag{18}$$

where

$$M(t) = \sum_{a=1}^{N} x_a(t) q_a(t) \tag{19}$$

and $x_a(t)$ and $q_a(t)$ are the position and charge of atom a at time t, respectively. The time derivative of the dipole moment is

$$\dot{M}(t) = \sum_{a=1}^{N} (v_a(t) q_a(t) + x_a(t)\dot{q}_a(t)) \tag{20}$$

where the second term on the right vanishes for simple, fixed-charge models like the Borodin force field.[39] An IR absorption spectrum computed from the same MD trajectory used to generate the phonon density of states (Figure 5) is presented in Figure 7 together with an experimental measurement from our laboratories. The agreement between the computed and measured spectra is rather poor because of the strong absorption at about 1900 cm^{-1} and the poor resolution of the -NO_2 symmetric and asymmetric stretches at about 1260 and 1650 cm^{-1}, respectively. For comparison, we have also calculated the IR absorption spectrum of single crystal ETN using the semiempirical DFTB method with the *lanl*31 parametrization.[40] These calculations were performed in a 1 × 3 × 1 supercell at 298 K with a time step for the integration of the equations of motion of 0.25 fs. The SCF-free Born–Oppenheimer MD formalism developed by Niklasson and co-workers was used estimate the self-consistent electronic ground state at each time step.[41] A 50,000 time step trajectory was

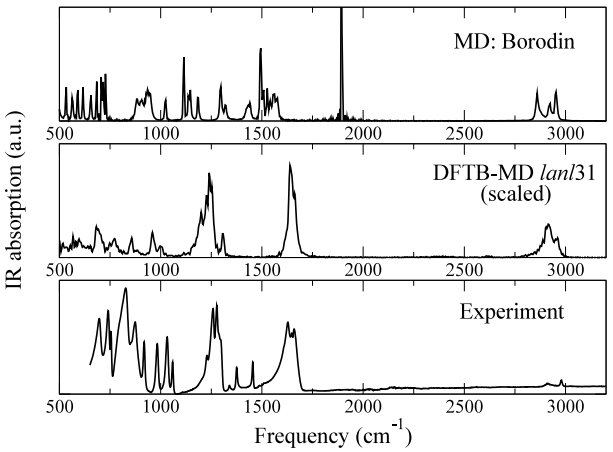

Figure 7. Infrared absorption spectra of single crystal ETN derived from the time history of the total dipole moment from classical MD trajectories at 300 K with the Borodin force field and semiempirical DFTB theory.

used to compute $I(\omega)$ and the $\dot{q}$ term in eq 18, which does not vanish in DFTB theory owing the self-consistent calculation of Mulliken partial changes at each time step, was evaluated by finite differences.[39] Like most quantum mechanical methods, DFTB-*lanl*31 systematically overestimates the normal-mode frequencies of organic molecules with respect to experiment (see, for example, ref 42). Hence, the frequencies presented in Figure 7 from the DFTB-MD simulations were rescaled uniformly by a factor of 0.92. The IR absorption spectrum derived from DFTB-MD is in better agreement with experiment than the spectrum computed from the Borodin force field. In particular, the two strong absorptions arising from the nitro groups are aligned well with those in the experimental spectrum. These analyses of the vibrational properties of the single crystal ETN indicate that while the Borodin force field provides a very good description of the intermolecular forces, its ability to describe accurately the intramolecular forces is comparatively limited.

3.3. Single Crystal Elastic Constants. The relationship between the second Piola–Kirchhoff elastic stress, τ_{ij}, and strain, η_{kl}, tensors in crystalline materials is described by the fourth rank tensor of second order elastic constants, C_{ijkl}, that is,

$$\tau_{ij} = C_{ijkl}\eta_{kl} \tag{21}$$

where the subscripts denote Cartesian directions.[43] The material-specific tensors of elastic constants, with a volumetric equation of state, are crucial components of single crystal plasticity models that are used in simulations of the thermomechanical response of energetic materials to mechanical loads (see, for example, refs 44–48). We have therefore used the Borodin force field to compute the 13 nonzero elastic constants of monoclinic ETN as a function of temperature between 200 and 400 K at zero external pressure. The dependence of the elastic constants on compression is more complex, especially under nonhydrostatic conditions, and is best described by an expansion of the elastic energy to higher orders in strain.

The elastic constants of a material can be derived from the fluctuations in the lattice vectors of the periodic simulation cell during an MD simulation in the isothermal–isobaric ensemble via the famous result of Parrinello and Rahman

https://doi.org/10.1021/acs.jpcc.4c00489
J. Phys. Chem. C 2024, 128, 5749–5758

$$\langle \eta_{ij}\eta_{kl}\rangle = \frac{k_B T}{\bar{V}} S_{ijkl} \tag{22}$$

where $\bar{V}$ is the mean volume of the simulation cell and S_{ijkl} the tensor of elastic compliances.[49−51] The MD simulations of single crystal ETN with the Borodin force field used a single Nose−Hoover-style thermostat and barostat in LAMMPS, that is, the variables tchain and pchain in the LAMMPS input were set to 1. The systems were initially thermalized for 10^6 time steps at each temperature. LAMMPS provides the six components of the three vectors that define the simulation cell, $v_a = (a_1,0,0)$, $v_b = (b_1, b_2,0)$, and $v_c = (c_1, c_2, c_3)$, which were written to file every 250 time steps throughout the production simulations. The production simulations were run for at least 1.6×10^7 time steps until the values of the elastic constants converged to a tolerance of 0.1 GPa.

The strain tensors, η, were computed from the thermal fluctuations of the three lattice vectors about their mean positions, $\bar{v}_a = (\bar{a}_1,0,0)$, $\bar{v}_b = (\bar{b}_1, \bar{b}_2,0)$, and $\bar{v}_c = (\bar{c}_1, \bar{c}_2, \bar{c}_3)$, where the bar denotes the time-average quantity over the whole production run. The mean volume of the simulation cell is $\bar{V} = \bar{a}_1\bar{b}_2\bar{c}_3$. The elements of matrix χ that transform the mean vectors, $\bar{v}_a$, $\bar{v}_b$, and $\bar{v}_c$, which represent the shape of the unstrained crystal at temperature T, to the instantaneous vectors, v_a, v_b, and v_c, at time step t are

$$\chi_{11}(t) = a_1(t)/\bar{a}_1$$
$$\chi_{12}(t) = b_1(t)/\bar{b}_1$$
$$\chi_{13}(t) = c_1(t)/\bar{c}_1$$
$$\chi_{22}(t) = b_2(t)/\bar{b}_2$$
$$\chi_{23}(t) = c_2(t)/\bar{c}_2$$
$$\chi_{33}(t) = c_3(t)/\bar{c}_3$$
$$\chi_{21}(t) = \chi_{31}(t) = \chi_{32}(t) = 0 \tag{23}$$

The corresponding Lagrangian strain tensor is

$$\eta_{ij} = \frac{1}{2}\left(\sum_k \chi_{ki}\chi_{kj} - \delta_{ij}\right) \tag{24}$$

where δ_{ij} is the Kronecker delta.[35] The Parrinello−Rahman strain fluctuation formula, eq 22, shows that time averages of the products of the Lagrangian strains yield the 81 elements of the elastic compliance tensor, S. The elastic constants (or stiffnesses) are calculated from the tensor of elastic compliances by transforming the fourth rank tensor to a 6×6 matrix using the Voigt contraction, $ij \rightarrow m$ and $kl \rightarrow n$, where $11 \rightarrow 1$, $22 \rightarrow 2$, $33 \rightarrow 3$, $12 \rightarrow 6$, $13 \rightarrow 5$, $23 \rightarrow 4$, and applying the relations $S_{mn} = S_{ijkl}$ if m and $n = 1, 2, 3$; $S_{mn} = 2S_{ijkl}$ if $m = 1, 2, 3$ and $n = 4, 5, 6$ or $m = 4, 5, 6$ and $n = 1, 2, 3$; $S_{mn} = 4S_{ijkl}$ if m and $n = 4, 5, 6$. The elastic constants, in Voigt notation, are obtained from the matrix of elastic compliances, S_{mn}, by a matrix inversion, $C = S^{-1}$.[35] The 13 nonvanishing elastic constants of single crystal ETN from 200 to 400 K are presented in Table 4 and Figure 8.

The stability of the lattice to the application of small strains requires that the combinations of elastic constants listed in eqs 26−38 of ref 52 should all be positive. These stability criteria are clearly satisfied for single crystal ETN over the temperature range 200−400 K because all of the elastic constants are individually positive and $C_{11} + C_{22} > 2C_{12}$, $C_{11} + C_{33} > 2C_{13}$, and $C_{22} + C_{33} > 2C_{23}$. The bulk modulus evaluated from the single crystal elastic constants,

$$K_0 = \frac{1}{9}(C_{11} + C_{22} + C_{33} + 2(C_{12} + C_{13} + C_{23})) \tag{25}$$

at 300 K is 6.89 GPa, which compares very favorably with the independent estimation of the isothermal bulk modulus through the fit of the MACAW reference curve to the room temperature isothermal compression curve, 6.78 GPa.

Table 4. Single Crystal Elastic Constants, C_{ij}, of ETN Computed from the Borodin Force Field with the Parrinello−Rahman Method between 200 and 400 K

(GPa)	200 K	250 K	300 K	350 K	400 K
C_{11}	14.8	13.5	12.3	10.5	9.0
C_{22}	6.7	5.6	4.7	3.8	3.3
C_{33}	19.2	17.2	15.9	13.5	11.3
C_{44}	4.7	4.3	3.9	3.5	3.1
C_{55}	1.1	1.0	0.9	0.8	0.6
C_{66}	5.2	4.9	4.2	4.0	3.7
C_{12}	5.7	5.0	4.6	3.9	3.8
C_{13}	5.7	5.3	4.8	3.7	3.3
C_{23}	6.1	5.5	5.2	4.4	4.0
C_{15}	1.4	1.3	1.1	0.9	0.8
C_{25}	1.5	1.3	1.2	1.1	1.0
C_{35}	4.6	4.2	3.9	3.3	2.7
C_{46}	2.2	2.1	1.9	2.0	2.0

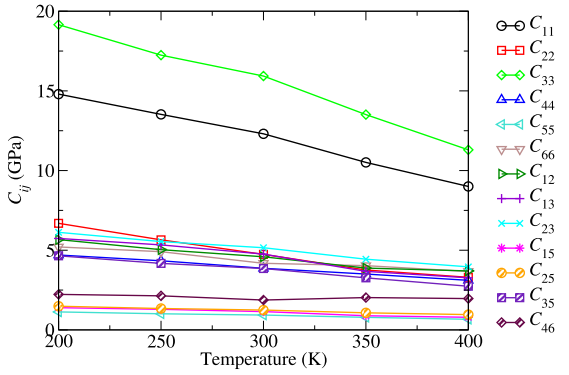

Figure 8. Dependence of the single crystal elastic constants of ETN on temperature.

3.4. Liquid viscosity. The drop weight impact test is used routinely to evaluate the handling safety of new explosives with respect to a well-characterized standard, such as PETN.[53−56] Many explosives have been observed to melt prior to ignition under the low-pressure, large-deformation conditions imparted by the test.[57−61] Viscous heating within the molten material and interruptions to the lateral flow of the liquid have been evaluated as potential ignition mechanisms by a number of groups since the 1940s.[54,62,63] Hence, we used the Borodin force field to evaluate the viscosity of liquid ETN and its dependence on temperature to inform continuum-level simulations of heat generation during high velocity flows.

The initial geometry for the simulations of liquid ETN was generated by placing 200 ETN molecules at random positions within a cubic simulation cell while avoiding close approaches between atoms. The volume of the supercell was set by requiring an initial density of 1.2 g/cm^3. The supercell was subsequently thermalized using isothermal−isobaric dynamics

https://doi.org/10.1021/acs.jpcc.4c00489
J. Phys. Chem. C 2024, 128, 5749−5758

to a target temperature and pressure of 500 K and 0 GPa, respectively. The thermalization was run for 7×10^5 time steps, which was more than sufficient for the temperature and density to reach their equilibrium values. The visualization of snap shots from the thermalization run confirmed that the molecules remained in a liquid-like state with no long-range order. Simulations of the density of liquid ETN at zero pressure were performed between 350 and 750 K by using isothermal−isobaric dynamics with this simulation cell as the starting point. The temperature dependence of the density of liquid ETN is presented in Figure 9, which shows that the

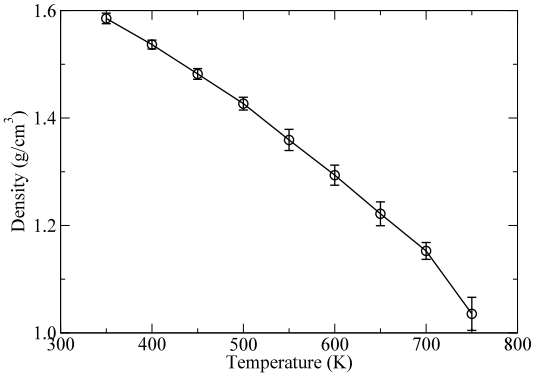

Figure 9. Temperature dependence of the density of liquid ETN at zero pressure from isothermal-isobaric molecular dynamics simulations with the Borodin force field.

density decreases quadratically with temperature between 350 and 700 K. Extrapolating these results to the experimentally measured melting temperature, T_m = 334 K, yields a density of 1.602 g/cm^3 at zero pressure.

The shear viscosity, μ, of liquid ETN at the densities and temperatures presented in Figure 9 were determined via the fluctuations in the off-diagonal, $i \neq j$, components of the virial stress tensor,

$$\mu_{ij} = \frac{V}{k_B T} \int_0^\infty \langle \sigma_{ij}(t)\sigma_{ij}(0)\rangle \mathrm{d}t \tag{26}$$

where

$$\sigma_{ij} = \frac{1}{V}\left(\sum_a p_{ai}p_{aj}/m_a + \frac{1}{2}\sum_a \sum_{b\neq a} r_{abi}f_{abj} \right) \tag{27}$$

and p_{ai} is the momentum of atom a in Cartesian direction i, m_a is the mass of atom a, and r_{abi} and f_{abi} are the i component of the position and force vectors between atoms a and b, repectively.[64]

Because we expect the properties of liquid ETN to be isotropic, $\mu_{12} = \mu_{13} = \mu_{23}$, the mean viscosity is $\bar{\mu} = (\mu_{12} + \mu_{13} + \mu_{23})/3$. Repeated indices in eq 26 are not summed over. The MD simulations were performed on cubic simulation cells containing 200 molecules in the canonical ensemble (constant number of particles, volume, and temperature) with a single Nose−Hoover thermostat. The correlation functions in eq 26 were evaluated over 4×10^7 time steps or 10 ns, which we found to be sufficient to give well-converged integrals.

It is common to represent the temperature dependence of the shear viscosity of liquids by Nahme's law

$$\mu(T) = \mu_0 \exp\left(\frac{-\beta(T - T_0)}{T_0} \right) \tag{28}$$

where β is a parameter to be fitted (see, for example, refs 63,65−67). We take $T_0 = T_m$ so that the constant μ_0 is equal to the shear viscosity of the system at the melting temperature. The three values for the shear viscosity obtained at each density and temperature from the MD simulations are plotted on a log−linear scale as a function of temperature in Figure 10, which clearly illustrates the efficacy of eq 28 as a description of $\mu(T)$. A linear regression to these data yields β = 3.98 and 0.0224 Pa s.

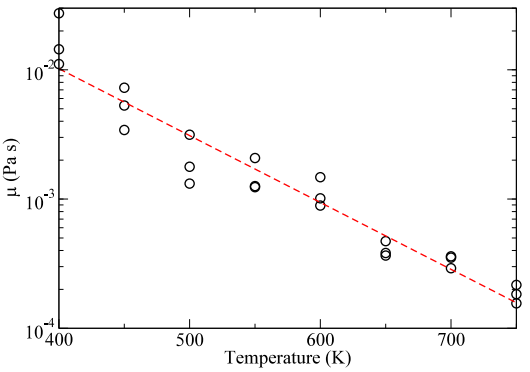

Figure 10. Shear viscosities calculated from the fluctuations in shear stresses for liquid ETN (symbols). The broken line denotes the best fit of Nahme's law (eq 28) to the data.

4. SUMMARY

The nonreactive force field for alkyl nitrates developed by Borodin and co-workers has been applied to MD simulations of the properties of crystalline and liquid ETN. The force field provides accurate predictions for the density and lattice parameters of single crystal ETN versus experimental data between 100 K and room temperature. The force field has then been applied in the calculation of the properties of ETN that are useful in the construction of an equation of state or a complete expansion of the Helmholtz free energy in terms of volumetric and deviatoric strains. These properties include the room temperature isothermal compression curve, linear and volumetric coefficients of thermal expansion, constant volume heat capacity, Grüneisen parameter, and single crystal elastic constants and their dependences on temperature. Despite the accurate representation of the structure of crystalline ETN at finite temperatures obtained from the force field, it fails to accurately describe its vibrational modes. Finally, because ETN is a melt-castable explosive and the properties of liquid explosives are important for understanding their ignition behavior during small scale safety testing, we have computed the temperature dependence of the density and shear viscosity of liquid ETN. We find that the temperature dependence of the shear viscosity can be represented accurately by Nahme's law.

Nonreactive force fields of this kind are applied frequently in large-scale MD simulations to understand the response of energetic molecular crystals to dynamic compression. These simulations have revealed the homogeneous nucleation of crystal defects including dislocations,[68−71] shear bands,[72,73] twins,[74] and other complex deformation mechanisms common

https://doi.org/10.1021/acs.jpcc.4c00489
J. Phys. Chem. C 2024, 128, 5749−5758

in highly anisotropic materials.[75−77] In addition, atomic-scale simulations under static or quasi-static conditions have been used to characterize the core structures of crystal defects and polymorphic phase transformations.[78−85] Hence, the force field for alkyl nitrates, which has been validated in this work for monoclinic ETN, may also be of value for characterizing the plasticity and phase stability of this and related materials under a variety of loading conditions.

■ ASSOCIATED CONTENT

Supporting Information

The Supporting Information is available free of charge at https://pubs.acs.org/doi/10.1021/acs.jpcc.4c00489.

LAMMPS input for the Bedrov force field (TXT)
LAMMPS input for an ETN supercell (TXT)

■ AUTHOR INFORMATION

Corresponding Author

M. J. Cawkwell − *Los Alamos National Laboratory, Los Alamos, New Mexico 87545, United States;* orcid.org/0000-0002-8919-3368; Email: cawkwell@lanl.gov

Author

V. W. Manner − *Los Alamos National Laboratory, Los Alamos, New Mexico 87545, United States;* orcid.org/0000-0002-1916-4887

Complete contact information is available at: https://pubs.acs.org/10.1021/acs.jpcc.4c00489

Notes

The authors declare no competing financial interest.

■ ACKNOWLEDGMENTS

We thank Kyle Spielvogel for providing the IR spectrum of solid ETN and Romain Perriot for useful discussions. Research presented in this article was supported by the Laboratory Directed Research and Development program of Los Alamos National Laboratory under project number 20220068DR. This research used resources provided by the Los Alamos National Laboratory Institutional Computing Program, which is supported by the U.S. Department of Energy National Nuclear Security Administration under Contract No. 89233218CNA000001.

■ REFERENCES

(1) Oxley, J. C.; Smith, J. L.; Brady, J. E.; Brown, A. C. Characterization and Analysis of Tetranitrate Esters. *Propellants Explos. Pyrotech.* **2012**, *37*, 24−39.

(2) Matyáš, R.; Künzel, M.; Ruzicka, A.; Knotek, P.; Vodochodsky, O. Characterization of Erythritol Tetranitrate Physical Properties. *Propellants Explos. Pyrotech.* **2015**, *40*, 185−188.

(3) McDonald, D. L.; Manner, V. W.; Tappan, B. C.; Lease, N.; Brown, G. W.; Mueller, A. Thermal stability of solid and molten erythritol tetranitrate (ETN). In *AIP Conference Proceedings*; AIP Publishing: 2020.

(4) Künzel, M.; Matyáš, R.; Vodochodsky, O.; Pachman, J. Explosive Properties of Melt Cast Erythritol Tetranitrate (ETN). *Cent. Eur. J. Energetic Mater.* **2017**, *14*, 418−429.

(5) Manner, V. W.; Tappan, B. C.; Scott, B. L.; Preston, D. N.; Brown, G. W. Crystal Structure, Packing Analysis, and Structural-Sensitivity Correlations of Erythritol Tetranitrate. *Cryst. Growth Des.* **2014**, *14*, 6154−6160.

(6) Manner, V. W.; Preston, D. N.; Tappan, B. C.; Sanders, V. E.; Brown, G. W.; Hartline, E.; Jensen, B. Explosive Performance Properties of Erythritol Tetranitrate (ETN). *Propellants Explos. Pyrotech.* **2015**, *40*, 460−462.

(7) Matyáš, R.; Lycka, A.; Jirásko, R.; Jakovy, Z.; Maixner, J.; Misková, L.; Künzel, M. Analytical Characterization of Erythritol Tetranitrate, an Improvised Explosive. *Journal of Forensic Sciences* **2016**, *61*, 759−764.

(8) Bezemer, K.; McLennan, L.; van Duin, L.; Kuijpers, C. J.; Koeberg, M.; von den Elshout, J.; van der Heijden, A.; Busby, T.; Yevdokimov, A.; Schoenmakers, P.; Smith, J.; Oxley, J.; van Asten, A. Chemical Attribution of the Home-Made Explosive ETN - Part I: Liquid Chromatography-Mass Spectrometry Analysis of Partially Nitrated Erythritol Impurities. *Forensic Sci. Int.* **2020**, *307*, No. 110102.

(9) Bezemer, K.; McLennan, L.; Hessels, R.; Schoorl, J.; van den Elshout, J.; van der Heijden, A.; Hulsbergen, A.; Koeberg, M.; Busby, T.; Yevdokimov, A.; de Rijke, E.; Schoenmakers, P.; Smith, J.; Oxley, J.; van Asten, A. Chemical Attribution of the Homemade Explosive ETN - Part II: Isotope Ratio Mass Spectrometry Analysis of ETN and Its Precursors. *For. Sci. Int.* **2020**, *313*, No. 110344.

(10) Freye, C. E.; Kinman, W. S.; Tiemann, C.; McDonald, D.; Manner, V. W.; Bowden, P. R.; Tappan, B. C.; Greenfield, M. T. Linking Chemical Precursors to the Synthesis of Erythritol Tetranitrate. *Forensic Chem.* **2020**, *19*, No. 100246.

(11) Oxley, J. C.; Furman, D.; Brown, A. C.; Dubnikova, F.; Smith, J. L.; Kosloff, R.; Zeiri, Y. Thermal Decomposition of Erythritol Tetranitrate: A Joint Experimental and Computational Study. *J. Phys. Chem. C* **2017**, *121*, 16145−16157.

(12) Cawkwell, M. J.; Ferriera, S. R.; Lease, N.; Manner, V. W., Ranking Explosive Sensitivity with Chemical Kinetics Derived from Molecular Dynamics Simulations. In *Molecular Modeling of the Sensitivities of Energetic Materials*, Mathieu, D., Ed. Elsevier: Amsterdam, 2021; Vol. *22*, pp 347−367.

(13) Cawkwell, M. J.; Davis, J. V.; Lease, N.; Marrs, F. W.; Burch, A. C.; Ferreira, S. R.; Manner, V. W. Understanding Explosive Sensitivity with Effective Trigger Linkage Kinetics. *ACS Phys. Chem. Au* **2022**, *2*, 448−458.

(14) Lease, N.; Klamborowski, L. M.; Perriot, R.; Cawkwell, M. J.; Manner, V. W. Identifying the Molecular Properties That Drive Explosive Sensitivity in a Series of Nitrate Esters. *J. Phys. Chem. Lett.* **2022**, *13*, 9422−9428.

(15) Lease, N.; Kay, L.; Chavez, D. E.; Robbins, D.; Manner, V. W. Increased Handling Sensitivity of Molten Erythritol Tetranitrate (ETN). *J. Hazard. Mater.* **2019**, *367*, 546−549.

(16) Moore, J. D.; Cheng, R. M.; Zecevic, M.; Holmes, M. D.; Cawkwell, M. J.; Manner, V. W. A High-Throughput Drop-Weight Impact Instrument for Imaging the Initiation and Propagation of Reactions in Energetic Materials. *AIP Conf. Proc.* **2023**, *2844*, 430002.

(17) Borodin, O.; Smith, G. D.; Sewell, T. D.; Bedrov, D. Polarizable and Nonpolarizable Force Fields for Alkyl Nitrates. *J. Phys. Chem. B* **2008**, *112*, 734−742.

(18) LAMMPS. https://www.lammps.org.

(19) Plimpton, S. Fast Parallel Algorithms for Short-Range Molecular-Dynamics. *J. Comput. Phys.* **1995**, *117*, 1−19.

(20) Hockney, R. W.; Eastwood, J. W. *Computer Simulation Using Particles*; IOP Publishing: Bristol, U.K., 1988.

(21) Elstner, M.; Porezag, D.; Jungnickel, G.; Elsner, J.; Haugk, M.; Frauenheim, T.; Suhai, S.; Seifert, G. Self-Consistent-Charge Density-Functional Tight-Binding Method for Simulations of Complex Materials Properties. *Phys. Rev. B* **1998**, *58*, 7260−7268.

(22) VandeVondele, J.; Krack, M.; Mohamed, F.; Parrinello, M.; Chassaing, T.; Hutter, J. Quickstep: Fast and Accurate Density Functional Calculations Using a Mixed Gaussian and Plane Waves Approach. *Comput. Phys. Commun.* **2005**, *167*, 103.

(23) Perdew, J. P.; Burke, K.; Ernzerhof, M. Generalized Gradient Approximation Made Simple. *Phys. Rev. Lett.* **1996**, *77*, 3865−3868.

(24) Goedecker, S.; Teter, M.; Hutter, J. Separable Dual-Space Gaussian Pseudopotentials. *Phys. Rev. B* **1996**, *54*, 1703.

(25) Grimme, S.; Ehrlich, S.; Goerigk, L. Effect of the Damping Function in Dispersion Corrected Density Functional Theory. *J. Comput. Chem.* **2011**, *32*, 1456.
(26) Monkhorst, H. J.; Pack, J. D. Special Points for Brillouin-Zone Integrations. *Phys. Rev. B* **1976**, *13*, 5188.
(27) Perriot, R. Pressure, Temperature, and Orientation Dependent Thermal Conductivity of Pentaerythritol Tetranitrate (PETN). *J. Appl. Phys.* **2021**, *130*, 225102.
(28) Perriot, R.; Cawkwell, M. J. Thermal Conductivity Tensor of β-1,3,5,7-Tetranitro-1,3,5,7-Tetrazoctane (β-HMX) as a Function of Pressure and Temperature. *J. Appl. Phys.* **2021**, *130*, 145106.
(29) Perriot, R.; Cawkwell, M. J. Thermal Conductivity Tensor of γ and ε-Hexanitrohexaazaisowurtzitane as a Function of Pressure and Temperature. *AIP Adv.* **2022**, *12*, No. 085203.
(30) Härtel, M. A. C.; Klapötke, T. M.; Stierstorfer, J.; Zehetner, L. Vapor Pressure of Linear Nitrate Esters Determined by Transpiration Method in Combination with VO-GC/MS. *Propellants Explos. Pyrotech.* **2019**, *44*, 484−492.
(31) Lozano, E.; Aslam, T. D. A Robust Three-Parameter Reference Curve for Condensed Phase Materials. *J. Appl. Phys.* **2022**, *131*, No. 015902.
(32) Lozano, E.; Cawkwell, M. J.; Aslam, T. D. An Analytic and Complete Equation of State for Condensed Phase Materials. *J. Appl. Phys.* **2023**, *134*, 125102.
(33) Bolotina, N. B.; Pinkerton, A. A. Temperature Dependence of Thermal Expansion Tensors of Energetic Materials. *J. Appl. Crystallogr.* **2015**, *48*, 1364−1380.
(34) Dickey, J. M.; Paskin, A. Computer Simulation of Lattice Dynamics of Solids. *Phys. Rev.* **1969**, *188*, 1407.
(35) Wallace, D. C. *Thermodynamics of Crystals*; Dover: Mineola, NY, 1998.
(36) Anderson, O. L. *Equations of State of Solids for Geophysics and Ceramic Science*; Oxford University Press: Oxford, 1995.
(37) Boulard, B.; Kieffer, J.; Phifer, C. C.; Angell, C. A. Vibrational Spectra in Fluoride Crystals and Glasses at Normal and High Pressures by Computer Simulation. *J. Non-Cryst. Solids* **1992**, *140*, 350−358.
(38) Praprotnik, M.; Janežič, D. Molecular Dynamics Integration and Molecular Vibrational Theory. Iii. The Infrared Spectrum of Water. *J. Chem. Phys.* **2005**, *122*, 174103.
(39) Bowlan, P.; Powell, M.; Perriot, R.; Martinez, E.; Kober, E. M.; Cawkwell, M. J.; McGrane, S. Probing Ultrafast Shock-Induced Chemistry in Liquids Using Broad-Band Mid-Infrared Absorption Spectroscopy. *J. Chem. Phys.* **2019**, *150*, 204503.
(40) Cawkwell, M. J.; Perriot, R. Transferable Density Functional Tight Binding for Carbon, Hydrogen, Nitrogen, and Oxygen: Application to Shock Compression. *J. Chem. Phys.* **2019**, *150*, No. 024107.
(41) Niklasson, A. M. N.; Cawkwell, M. J. Fast Method for Quantum Mechanical Molecular Dynamics. *Phys. Rev. B* **2012**, *86*, No. 174308.
(42) Alecu, I. M.; Zheng, J.; Zhao, Y.; Truhlar, D. G. Computational Thermochemistry: Scale Factor Databases and Scale Factors for Vibrational Frequencies Obtained from Electronic Model Chemistries. *J. Chem. Theory Comput.* **2010**, *6*, 2872−2887.
(43) Nye, J. F. *Physical Properties of Crystals*; Clarendon: Oxford, 1967.
(44) Luscher, D. J.; Addessio, F. L.; Cawkwell, M. J.; Ramos, K. J. A Dislocation Density-Based Continuum Model of the Anisotropic Shock Response of Single Crystal Alpha-Cyclotrimethylene Trinitramine. *J. Mech. Phys. Solids* **2017**, *98*, 63−86.
(45) Addessio, F. L.; Luscher, D. J.; Cawkwell, M. J.; Ramos, K. J. A Single-Crystal Model for the High-Strain Rate Deformation of Cyclotrimethylene Trinitramine Including Phase Transformations and Plastic Slip. *J. Appl. Phys.* **2017**, *121*, 185902.
(46) Zecevic, M.; Cawkwell, M. J.; Ramos, K. J.; Luscher, D. J. Crystal Plasticity Including a Phase-Field Deformation Twinning Model for the High-Rate Deformation of Cyclotetramethylene Tetranitramine. *J. Mech. Phys. Solids* **2022**, *163*, No. 104872.
(47) Barton, N. R.; Winter, N. W.; Reaugh, J. E. Defect Evolution and Pore Collapse in Crystalline Energetic Materials. *Modell. Simul. Mater. Sci. Eng.* **2009**, *17*, No. 035003.
(48) Duarte, C. A.; Koslowski, M. Hot-Spots in Polycrystalline Beta-Tetramethylene Tetranitramine (Beta-HMX): The Role of Plasticity and Friction. *J. Mech. Phys. Solids* **2023**, *171*, No. 105157.
(49) Parrinello, M.; Rahman, A. Strain Fluctuations and Elastic Constants. *J. Chem. Phys.* **1982**, *76*, 2662.
(50) Sprik, M.; Impey, R. W.; Klein, M. L. Second-Order Elastic Constants for the Lennard-Jones Solid. *Phys. Rev. B* **1984**, *29*, 4368.
(51) Hooks, D. E.; Ramos, K. J.; Bolme, C. A.; Cawkwell, M. J. Elasticity of Crystalline Molecular Explosives. *Propellants Explos. Pyrotech.* **2015**, *40*, 333−350.
(52) Cawkwell, M. J.; Zecevic, M.; Luscher, D. J.; Ramos, K. J. Dependence of the Elastic Stiffness Tensors of PETN, α-RDX, γ-RDX, ε-RDX, ε-CL-20, DAAF, FOX-7, and β-HMX on Hydrostatic Compression. *Propellants, Explos., Pyrotech.* **2022**, *47*, No. e202100281.
(53) Marrs, F. W.; Manner, V. W.; Burch, A. C.; Yeager, J. D.; Brown, G. W.; Kay, L. M.; Buckley, R. T.; Anderson-Cook, C. M.; Cawkwell, M. J. Sources of Variation in Drop-Weight Impact Sensitivity Testing of the Explosive Pentaerythritol Tetranitrate. *Ind. Eng. Chem. Res.* **2021**, *60*, 5024−5033.
(54) Rae, P. J.; Dickson, P. M. Some Observations About the Drop-Weight Explosive Sensitivity Test. *J. Dyn. Behav. Mater.* **2021**, *7*, 414−424.
(55) Storm, C. B.; Stine, J. R.; Kramer, J. F. Sensitivity Relationships in Energetic Materials. *Chem. Phys. Energ. Mater.* **1990**, *309*, 605−639, DOI: 10.1007/978-94-009-2035-4_27.
(56) Gibbs, T. R.; Popolato, A. *LASL Explosives Properties Data*; University of California Press: 1980.
(57) Field, J. E.; Swallowe, G. M.; Heavens, S. N. Ignition Mechanisms of Explosives During Mechanical Deformation. *Proc. R. Soc. London, Ser. A* **1982**, *382*, 231−244.
(58) Heavens, S. N.; Field, J. E. Flow, Melting and Ignition of Solid Explosives under Impact. *Combust. Flame* **1972**, *18*, 473.
(59) Heavens, S. N.; Field, J. E. Ignition of a Thin-Layer of Explosive by Impact. *Proc. R. Soc. London, Ser. A* **1974**, *338*, 77.
(60) Mohan, V. K.; Field, J. E. Impact Initiation of Hexanitrostilbene. *Combust. Flame* **1984**, *56*, 269−277.
(61) Walley, S. M.; Field, J. E.; Biers, R. A.; Proud, W. G.; Williamson, D. M.; Jardine, A. P. The Use of Glass Anvils in Drop-Weight Studies of Energetic Materials. *Propellants Explos. Pyrotech.* **2015**, *40*, 351−365.
(62) Eirich, F. R.; Tabor, D. Collisions through Liquid Films. *Math. Proc. Camb. Philos. Soc.* **1948**, *44*, 566−580.
(63) Yuan, H.; Prosperetti, A. Transient Viscous Heating of Liquid Layers under Intense Shear. *Proc. R. Soc. London, Ser. A* **1996**, *352*, 2767−2783.
(64) Allen, M. P.; Tildesley, D. J. *Computer Simulation of Liquids*; Oxford University Press: Oxford, 1987.
(65) Sukanek, P. C. Poiseuille Flow of a Power-Law Fluid with Viscous Heating. *Chem. Eng. Sci.* **1971**, *26*, 1775−1776.
(66) Eldabe, N. T. M.; El-Sabbagh, M. F.; El-Sayed(Hajjaj), M. A.-S. The Stability of Plane Couette Flow of a Power-Law Fluid with Viscous Heating. *Phys. Fluids* **2007**, *19*, No. 094107.
(67) Costa, A.; Macedonio, G. Viscous Heating in Fluids with Temperature-Dependent Viscosity: Implications for Magma Flows. *Nonlinear Process. Geophys.* **2003**, *10*, 545−555.
(68) Jaramillo, E.; Sewell, T. D.; Strachan, A. Atomic-Level View of Inelastic Deformation in a Shock Loaded Molecular Crystal. *Phys. Rev. B* **2007**, *76*, No. 064112.
(69) Cawkwell, M. J.; Ramos, K. J.; Hooks, D. E.; Sewell, T. D. Homogeneous Dislocation Nucleation in Cyclotrimethylene Trinitramine under Shock Loading. *J. Appl. Phys.* **2010**, *107*, No. 063512, DOI: 10.1063/1.3305630.
(70) Ramos, K. J.; Hooks, D. E.; Sewell, T. D.; Cawkwell, M. J. Anomalous Hardening under Shock Compression in (021)-Oriented

Cyclotrimethylene Trinitramine Single Crystals. *J. Appl. Phys.* **2010**, *108*, No. 066105.
(71) Eason, R. M.; Sewell, T. D. Shock-Induced Inelastic Deformation in Oriented Crystalline Pentaerythritol Tetranitrate. *J. Phys. Chem. C* **2012**, *116*, 2226−2239.
(72) Cawkwell, M. J.; Sewell, T. D.; Zheng, L.; Thompson, D. L. Shock-Induced Shear Bands in an Energetic Molecular Crystal: Application of Shock-Front Absorbing Boundary Conditions to Molecular Dynamics Simulations. *Phys. Rev. B* **2008**, *78*, No. 014107.
(73) Izvekov, S.; Rice, B. M. Microscopic Mechanism of Nanoscale Shear Bands in an Energetic Molecular Crystal (α-RDX): A First-Order Structural Phase Transition. *Phys. Rev. B* **2022**, *106*, No. 104109.
(74) Pereverzev, A. Molecular Dynamics Study of Diffusionless Phase Transformations in HMX: β-HMX Twinning and β-ϵ Phase Transition. *J. Appl. Phys.* **2023**, *134*, 125105.
(75) Lafourcade, P.; Denoual, C.; Maillet, J. B. Irreversible Deformation Mechanisms for 1,3,5-Triamino-2,4,6-Trinitrobenzene Single Crystal through Molecular Dynamics Simulations. *J. Phys. Chem. C* **2018**, *122*, 14954−14964.
(76) Lafourcade, P.; Denoual, C.; Maillet, J. B. Mesoscopic Constitutive Law with Nonlinear Elasticity and Phase Transformation for the Twinning-Buckling of TATB under Dynamic Loading. *Phys. Rev. Mater.* **2019**, *3*, No. 053610.
(77) Lafourcade, P.; Maillet, J. B.; Bruzy, N.; Denoual, C. Molecular Dynamics Informed Calibration of Crystal Plasticity Critical Shear Stresses for the Mesoscopic Mechanical Modeling of 1,3,5-Triamino-2,4,6-Trinitrobenzene (TATB) Single Crystal. *J. Appl. Phys.* **2024**, *135*, No. 075901.
(78) Josyula, K.; Rahul; De, S. In Silico Study of α-γ Phase Transformation in Hexahydro-1,3,5-Trinitro-1,3,5-Triazine. *Comput. Mater. Sci.* **2019**, *170*, No. 109180, DOI: 10.1016/j.commatsci.2019.109180.
(79) Mathew, N.; Picu, R. C. Molecular Conformational Stability in Cyclotrimethylene Trinitramine Crystals. *J. Chem. Phys.* **2011**, *135*, No. 024510.
(80) Mathew, N.; Picu, R. C. Slip Asymmetry in the Molecular Crystal Cyclotrimethylenetrinitramine. *Chem. Phys. Lett.* **2013**, *582*, 78−81.
(81) Munday, L. B.; Chung, P. W.; Rice, B. M.; Solares, S. D. Simulations of High-Pressure Phases in RDX. *J. Phys. Chem. B* **2011**, *115*, 4378−4386.
(82) Munday, L. B.; Mitchell, R. L.; Knap, J.; Chung, P. W. Role of Molecule Flexibility on the Nucleation of Dislocations in Molecular Crystals. *Appl. Phys. Lett.* **2013**, *103*, 151911.
(83) Munday, L. B.; Solares, S. D.; Chung, P. W. Generalized Stacking Fault Energy Surfaces in the Molecular Crystal α-RDX. *Philos. Mag.* **2012**, *92*, 3036−3050.
(84) Pal, A.; Picu, C. R. Contribution of Molecular Flexibility to the Elastic-Plastic Properties of Molecular Crystal α-RDX. *Modell. Simul. Mater. Sci. Eng.* **2017**, *25*, No. 015006.
(85) Pal, A.; Picu, R. C. Rotational Defects in Cyclotrimethylene Trinitramine (RDX) Crystals. *J. Chem. Phys.* **2014**, *140*, No. 044512.

https://doi.org/10.1021/acs.jpcc.4c00489
J. Phys. Chem. C 2024, 128, 5749−5758